Distinct Mechanism for the Formation of the Ribonucleoprotein Complex of Tomato Spotted Wilt Virus

Yu Guo,[a,g] Baocheng Liu,[a] Zhenzhen Ding,[a] Guobang Li,[a,g] Meizi Liu,[a] Dantong Zhu,[f] Yuna Sun,[d] Shishang Dong,[a,c] Zhiyong Lou[b,e,g]

State Key Laboratory of Medicinal Chemical Biology and College of Pharmacy, Nankai University, Tianjin, China[a]; MOE Laboratory of Protein Science, School of Medicine, Tsinghua University, Beijing, China[b]; School of Biological Science and Technology, University of Jinan, Jinan, China[c]; National Laboratory of Macromolecules, Institute of Biophysics, Chinese Academy of Science, Beijing, China[d]; Collaborative Innovation Center for Biotherapy, Tsinghua University, Beijing, China[e]; High School Affiliated to Renmin University, Beijing, China[f]; Drug Discovery Center for Infectious Disease, Nankai University, Tianjin, China[g]

ABSTRACT The *Tomato spotted wilt virus* (TSWV) belongs to the *Tospovirus* genus of the *Bunyaviridae* family and represents the sole plant-infecting group within bunyavirus. TSWV encodes a nucleocapsid protein (N) which encapsidates the RNA genome to form a ribonucleoprotein complex (RNP). In addition, the N has multiple roles during the infection of plant cells. Here, we report the crystal structure of the full-length TSWV N. The N features a body domain consisting of an N-lobe and a C-lobe. These lobes clamp a positively charged groove which may constitute the RNA binding site. Furthermore, the body domains are flanked by N- and C-terminal arms which mediate homotypic interactions to the neighboring subunits, resulting in a ring-shaped N trimer. Interestingly, the C terminus of one protomer forms an additional interaction with the protomer of an adjacent trimer in the crystal, which may constitute a higher-order oligomerization contact. In this way, this study provides insights into the structure and trimeric assembly of TSWV N, which help to explain previous functional findings, but also suggests distinct N interactions within a higher-order RNP.

IMPORTANCE TSWV is one of the most devastating plant pathogens that cause severe diseases in numerous agronomic and ornamental crops worldwide. TSWV is also the prototypic member of the *Tospovirus* genus, which is the sole group of plant-infecting viruses in the bunyavirus family. This study determined the structure of full-length TSWV N in an oligomeric state. The structural observations explain previously identified biological properties of TSWV N. Most importantly, the additional homotypic interaction between the C terminus of one protomer with another protomer indicates that there is a distinct mechanism of RNP formation in the bunyavirus family, thereby enhancing the current knowledge of negative-sense single-stranded RNA virus-encoded N. TSWV N is the last remaining representative N with an unknown structure in the bunyavirus family. Combined with previous studies, the structure of TSWV N helps to build a complete picture of the bunyavirus-encoded N family and reveals a close evolutionary relationship between orthobunyavirus, phlebovirus, hantavirus, and tospovirus.

KEYWORDS RNP formation, tomato spotted wilt virus, crystal structure, nucleocapsid protein, oligomerization

Address correspondence to Shishang Dong, shishang_dong@126.com, or Zhiyong Lou, louzy@mail.tsinghua.edu.cn.

Y.G. and B.L. contributed equally to this article.

Bunyaviruses are the largest negative-sense single-stranded RNA (−ssRNA) virus family; the family contains more than 350 species (1). All bunyaviruses have a trisegmented genome, including large (L), middle (M), and small (S) segments. The L

segment encodes an RNA-dependent RNA polymerase (RdRp), the M segment encodes a precursor of glycoproteins (GPC), and the S segment encodes a nucleocapsid protein (N). A few *Bunyaviridae* members possess a nonstructural protein (NSs and/or NSm) that uses an ambisense coding strategy by the S and M segments (1). In a typical −ssRNA virus, the genomic RNAs of a bunyavirus are encapsidated by N to form a ribonucleoprotein (RNP) complex together with RdRp, and this complex has a central role in virus replication and transcription. Therefore, the understanding of how N encapsidates RNA and oligomerizes to form RNP is important for dissecting the molecular mechanism underlying the bunyavirus life cycle.

In a previous taxonomy, the *Bunyaviridae* family was subdivided into five distinct genera, namely the *Orthobunyavirus*, *Nairovirus*, *Phlebovirus*, *Hantavirus*, and *Tospovirus* genera. There is a wide diversity in the structures and functions of bunyavirus-encoded N proteins (NPs). For example, the molecular size of N encoded by Crimean-Congo hemorrhagic fever virus (CCHFV) in the *Nairovirus* genus is 52 kDa, but N encoded by Bunyamwera virus (BUNV) in the *Orthobunyavirus* genus is only 27 kDa (2, 3). An unexpected endonuclease activity was found in CCHFV N and Sin Nombre virus (SNV; in the *Hantavirus* genus) N but not in other bunyaviral N proteins (2, 4). A systematic study of all representative bunyaviral N proteins will elucidate their mechanisms in the virus life cycle. Since 2010, the structures of N proteins encoded by phlebovirus (Rift Valley fever virus [RVFV] and severe fever with thrombocytopenia syndrome virus [SFTSV]) (5–8), nairovirus (CCHFV) (2, 9, 10), orthobunyavirus (Schmallenberg virus [SBV], La Crosse orthobunyavirus [LACV], and BUNV) (3, 11, 13, 14), and hantavirus (SNV and Hantaan virus [HTNV]) (15, 16) have been successfully studied. However, the structure of tospovirus-encoded N remains exclusive.

Tomato spotted wilt virus (TSWV) is the prototypic member of the *Tospovirus* genus. It was first identified in Australia in 1915, causes serious diseases in numerous agronomic and ornamental crops around the world, and is one of the most devastating plant viruses (17). The *Tospovirus* genus is the sole group of plant-infecting viruses in the bunyavirus family, and it infects over 800 different plant species from 82 different families (1, 18). In the most recent update of the International Committee on Taxonomy of Viruses (ICTV), bunyaviruses were reclassified as a new *Bunyavirales* order that includes 9 virus families (19). In this recent taxonomy, tospoviruses are part of the *Orthotospovirus* genus within the *Tospoviridae* family.

N is one of the major structural proteins that assembles the TSWV RNP and has also been reported to have multiple biological functions in the virus life cycle. For example, a unique feature of plant-infecting viruses is that they invade the neighbor cells through cell wall connections known as plasmodesmata, and they reach distal parts of the plant through the vascular tissue after the establishment of infection in the initial infected plant cells (20, 21). The cell-to-cell transport of TSWV occurs through tubular structures derived from the NSm and is highly dependent on the correct interaction between NSm and N (22–24). Many biochemical and computational studies have been launched to investigate the relationship between the structure and function of TSWV N. For example, TSWV N was reported to form a range of higher-ordered oligomers in a head-to-tail interaction fashion (25, 26). Homologous structure modeling based on other reported bunyaviral N proteins suggested that key positively charged residues are responsible for binding to single-stranded RNA (25, 27). However, the structure of TSWV N and the mechanisms for N oligomerization and RNA encapsidation remain unclear. In particular, because bunyavirus-encoded N proteins show significant variations, it is necessary to acquire the experimental structure of TSWV N to determine whether the plant-infecting bunyavirus has a distinct mechanism for RNP formation.

RESULTS

Structure of TSWV N. The full-length TSWV N was expressed in *Escherichia coli*. Two mutations, R94A and R95A, were introduced to optimize the solution property of TSWV N for purification, crystallization, and structure determination, as suggested previously (25). The initial wild-type (WT) protein was analyzed by gel filtration and eluted as a
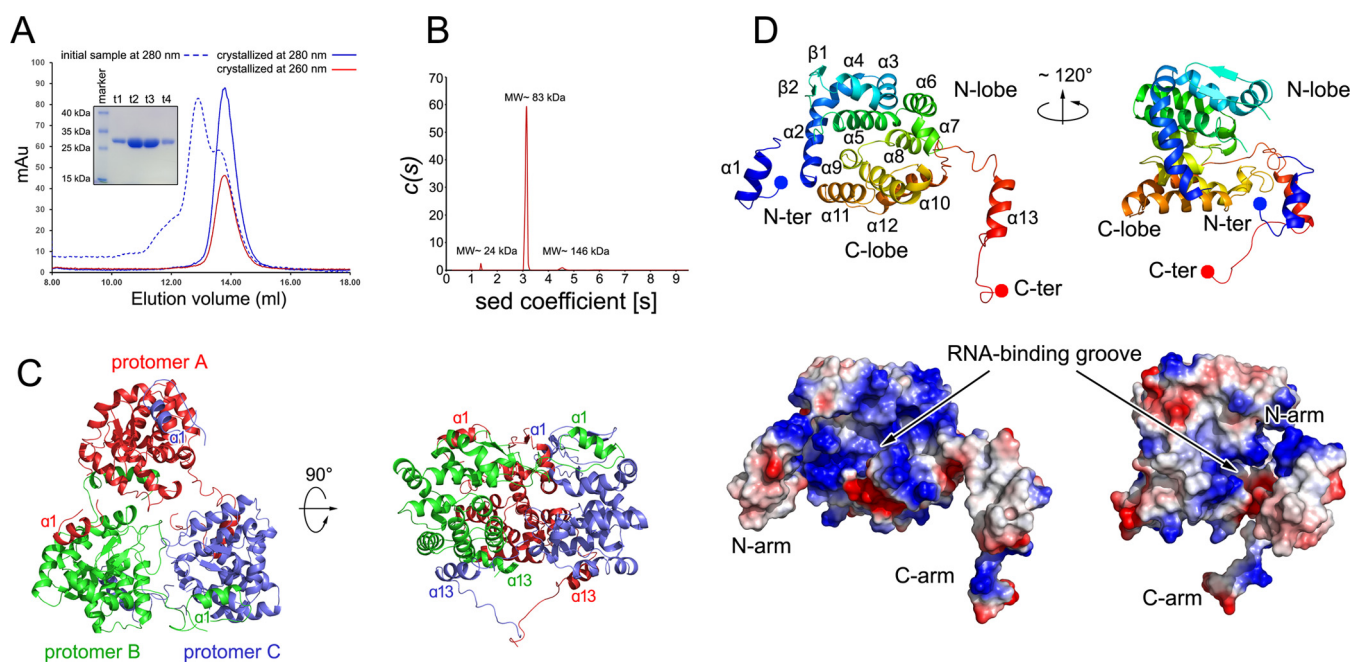
FIG 1 Structures of Sin Nombre virus (SNV) N and Andes virus (ANDV) N proteins. (A and B) Size exclusion chromatogram (SEC) and analytical ultracentrifuge (AUC) analysis of *E. coli*-expressed TSWV N. (A) SEC analysis of the initial sample and the crystallized sample was performed using a Superdex-200 10/300 column. The blue and red lines indicate absorbance of the crystallized sample at 280 nm and 260 nm, respectively. The dashed blue line indicates absorbance of the initial sample at 280 nm. The inset shows a 12% SDS-PAGE gel of the peak in SEC of the final sample. (B) The calculated molecular weights corresponding to each peak in AUC are labeled above the curve. sed, sedimentation. (C) Overall structure of the trimeric TSWV N in one crystallographic ASU in two perpendicular views. Three protomers are shown in the cartoon diagram and are colored red, green, and blue. (D) Ribbon representations of the TSWV N monomer (protomer B) with a rainbow coloring from the N terminus (blue) to the C terminus (red) are shown in two perpendicular views. Each structural portion and secondary structural element are labeled. Electrostatic surfaces are shown with the same orientation as that of the cartoon models. Positive and negative charges are indicated by blue and red, respectively.

continuous peak ranging from 12 to 15 ml on a Superdex-200 10/300 column, indicating a mixed oligomeric state (Fig. 1A). Since the initial sample could not be crystallized, we introduced the R94A R95A double mutation and purified the initial sample by a heparin column to remove the higher-order and inhomogeneous fraction, followed by a further purification on a gel filtration column. The further purified TSWV N displayed an oligomeric state in a single peak in gel filtration at an elution volume of 14 ml with an optical density (optical density at 260 nm [OD_{260}]/OD_{280}) value of 0.55, which indicates that there is a homogeneous oligomeric state without nucleic acid binding (Fig. 1A). Analytical ultracentrifugation analyses resulted in a molecular mass of 83 kDa for the purified species, which is consistent with a trimer (the molecular weight of the monomer is 28 kDa) (Fig. 1B). A previous study has shown that the *E. coli*-expressed TSWV N exists in oligomeric forms ranging from a monomer to a pentamer in solution (25). However, the reported monomeric and oligomeric forms present only negligible peaks in the analytical ultracentrifugation (AUC) results. This outcome might be caused by different expression and purification protocols.

Purified TSWV N was crystallized in a P2$_1$ space group. The structure was determined by a single-wavelength dispersion (SAD) method using a selenomethionine derivative and refined to a 2.8-Å resolution with R_{work}/R_{free} of 0.230/0.269 (see Table 2). Consistent with the AUC result, there are three protomers in the crystallographic asymmetric unit (ASU) that form a ring-shaped architecture in a head-to-head mode (Fig. 1C). A positively charged binding groove is located on the inner side of the ring and may comprise the RNA binding site.

Each N protomer has a compact body part flanked by extended N- and C-terminal arms that are comprised of 13 α-helices and 2 β-strands (Fig. 1D). The body part contains two separate domains: an N-lobe (A26 to S158) and a C-lobe (L159 to P224). The N-lobe is mainly composed of a helical core containing α2 to α9 attached by two

TABLE 1 Structure comparison of TSWV NP with other bunyavirus-encoded NPs

Target for comparison	PDB code	No. of Cα atoms of aligned residues	Z-score	RMSD (Å)
BUNV NP	4IJS	189	12.7	3.6
RVFV NP	4H5M	131	2.9	6.1
SNV NP	5E05	159	6.4	3.9

additional β-strands (β1 and β2) in an antiparallel manner. The C-lobe is smaller than the N-lobe and is comprised of three helices (α10 to α12). The N- and C-lobes clamp a highly positively charged crevice (Fig. 1D) that, in analogy to other reported N structures, may constitute the RNA binding site (see below). The N- and C-terminal arms extend out from the body and interact with the neighboring protomers for homotypic interaction.

Previous studies suggest that the folding of bunyavirus-encoded N proteins presents distinct features compared to that of other −ssRNA virus-encoded N proteins (15). Similarly, TSWV N displays less structural homology with N proteins encoded by viruses outside the bunyavirus family according to a search in the DALI server (28). In contrast, TSWV N presents molecular folding similar to that of other representative bunyaviral N proteins (Table 1), except for CCHFV N. The most significant matches based on the highest Z-scores and the lowest root mean square deviations (RMSD) are the N proteins encoded by orthobunyaviruses, including BUNV (PDB code 4IJS), Leanyer virus (PDB code 4J1J), Schmallenberg virus (PDB code 4JNG), and La Crosse virus (PDB code 4BGP) (3, 11, 13, 29). The Z-score for comparison of the body parts of TSWV N and orthobunyavirus N proteins is high, at 12.7, and the RMSD of Cα atoms of 189 aligned residues is low, at 3.6 Å, which indicates that high structural similarities exist between these proteins (Fig. 2). Both TSWV N and orthobunyavirus N proteins have a body part flanked by N- and C-terminal arms. Interestingly, primary sequence alignment suggests that the sequences of TSWV N and BUNV N are also partly related; in particular, residues involved in interprotomer interactions and RNA binding are highly conserved (Fig. 2B). Additionally, TSWV N is also homologous to N proteins encoded by phleboviruses, including RVFV (PDB code 4H5L) (5–7), SFTSV (PDB code 4J4X) (8), and Toscana virus (PDB code 4CSG) (30), with Z-scores ranging from 3 to 7 and the RMSD of Cα atoms of aligned residues ranging from 4 to 6 Å (Fig. 2A). However, no sequence identity was found between N proteins of TSWV and hantavirus. The largest variations of all these N proteins appear at N- and C-terminal arms. Both N- and C-terminal arms exist in TSWV N and orthobunyavirus N proteins, but the C terminus of phlebovirus and hantavirus N proteins ends in the body part and does not form an extended structure to make contact with adjacent protomers.

Flexibility of N- and C-terminal arms of TSWV N. Although the body parts of three protomers in one ASU are strictly conserved, with RMSD of less than 0.3 Å, a few significant structural shifts were observed. The major difference between nonequivalent protomers occurs in the conformation of the flexible hinges that place N- and C-terminal arms in different positions (Fig. 3A) while conserving the same arm-body interactions in the structure. In protomer B, the N-terminal arm is extended away from the body part and all residues can be traced in the electron density, whereas for protomers A and C, the N-terminal arm folds toward the body part and the hinge residues D20 to E25 cannot be traced. Moreover, β1 and β2 in the N-lobe fold close to the body part in protomer B compared to parts in protomers A/C (Fig. 3B). Unlike the missing linkage connecting the N-terminal arm, all C-terminal arms of three protomers show a clear connection to the body part. In addition to their different intersection angles with body parts, the C terminus up to the last residue, A258, of the protomers A/C has well-defined electron density, but K250 to A258 of protomer B cannot be defined due to the lack of density (which will be discussed in detail later). The stable conformations of the C-terminal arms of the protomers A/C are caused by the interaction of the C terminus with adjacent trimers in other ASUs. The different conforma-
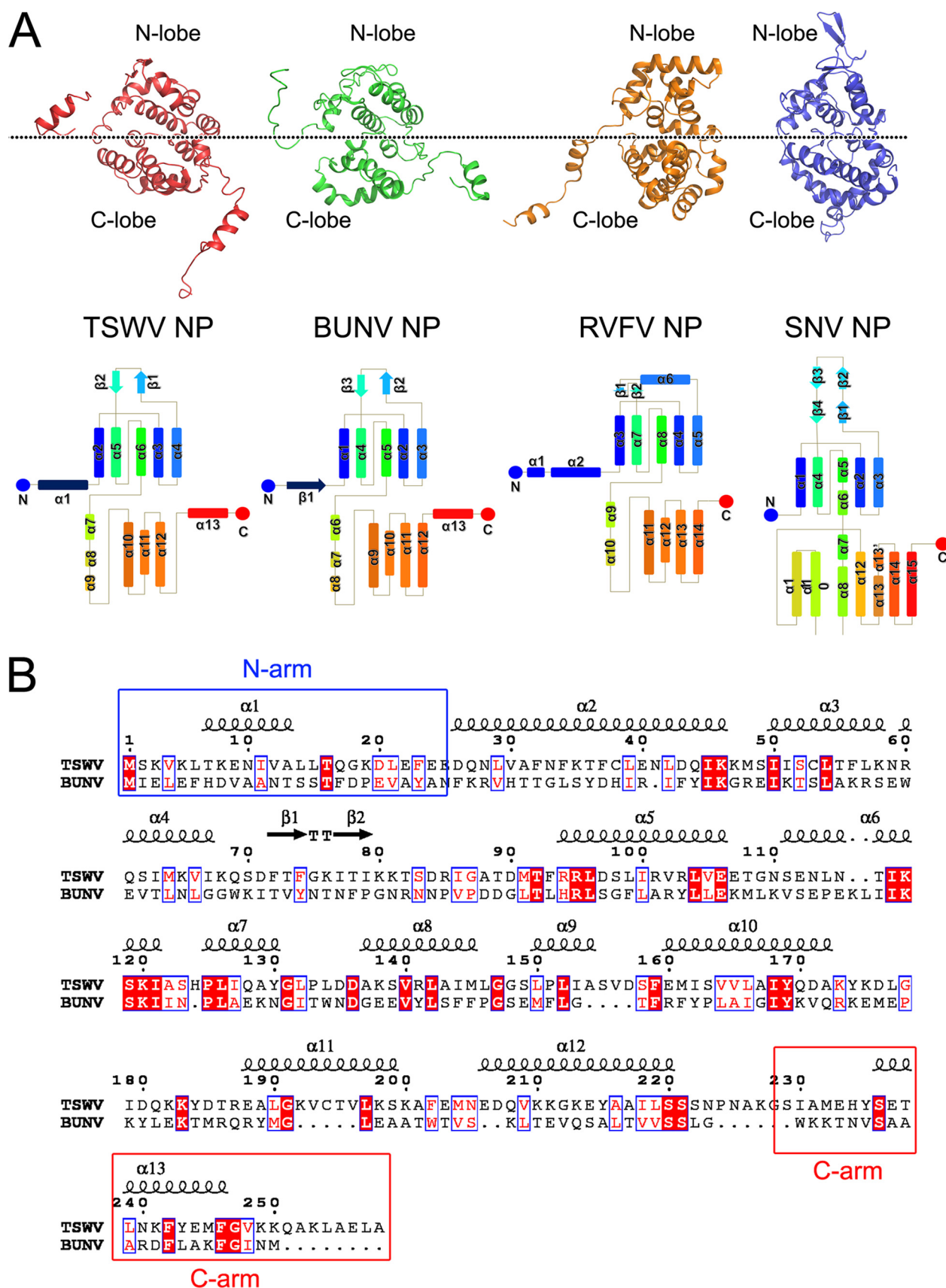
FIG 2 Comparison of hantavirus N with orthobunyavirus and phlebovirus N proteins. (A) The structures of TSWV N, BUNV N, RVFV N, and SNV N are aligned and shown in the same orientation. The polypeptides of the four N proteins are displayed in red, green, orange, and blue, respectively. The
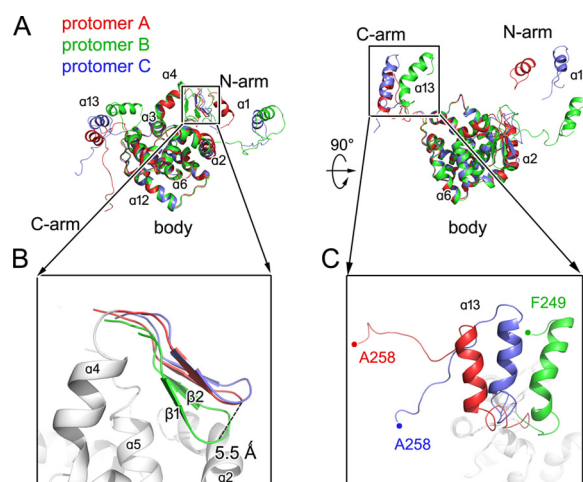
(Continued on next page)

FIG 3 Comparison of three protomers in the crystal structure. (A) Three protomers in one crystallographic ASU are aligned together. They are represented by red, green, and blue, and they are displayed in two perpendicular views. (B and C) Enlarged figures show the structural variations of β-strands in the N-terminal arm (B) and in the C-terminal arm (C).

tions of the N- and C-terminal arms are very likely caused by the different positions of each protomer in the ring-shaped oligomer, and this flexibility may allow the formation of higher-order RNPs *in vivo*.

Interprotomer interactions within the TSWV N trimer. Although various types of protomer folding can be observed, the interprotomer interactions within one N trimer are almost identical (Fig. 4). The interprotomer interactions exist in two separate regions (Fig. 4A): (i) the N-terminal region, where α1 (spanning residues T7 to L14) in the N-terminal arm of protomer A interacts with the N-lobe of a neighboring protomer C, and (ii) the C-terminal region, where α13 (spanning residues S234 to F246) in the C-terminal arm of protomer A interacts with the C-lobe of a neighboring protomer B.

The N-terminal interprotomer interaction occurs between the N-terminal arm of protomer A and the N-lobe of protomer B. α3, α4, and β1 of protomer B form a planar surface to bear the contact with the N-terminal arm of protomer A. The side chain and main chain atoms of residues K5, K8, E9, I11, V12, L14, L15, and Q17 of protomer A constitute a complex hydrogen bond network with additional hydrophobic contact with α3/α4/β1 in protomer B to stabilize the interaction of protomer A/B. K5 of protomer A is stabilized by the Oγ atom of S70 and backbone atoms of D71 in protomer B. K11 of protomer A forms a weak hydrogen bond with V66 of protomer B. The side chain of E9 in protomer A forms contacts with backbone atoms of T73 and F74 of protomer B. The conformation of E71 of protomer A is stabilized by the side chains of K58 and N59 of protomer B. I11, V12, L14, and L15 of protomer A also form hydrophobic contacts with protomer B.

The C-terminal interprotomer interaction occurs between the C-terminal arm of protomer A and the C-lobe of protomer C. A subset of hydrophobic residues in α10, α11, and α12 of protomer C forms a deep groove to accommodate the hydrophobic side chains of residues M232, Y235, L238, L239, F242, Y243, M245, and F246 of protomer A. Additionally, a subset of hydrogen bonds connecting the side chain of E234 and the main atoms of α13 in protomer A with the C-lobe of protomer B helps to stabilize this C-terminal interaction.

FIG 2 Legend (Continued)
topologies of the N proteins (NP) are shown in the lower panels. Helices and strands are represented by rectangles and arrows, respectively, and they are rainbow colored, with blue and red indicating the N- and C-terminal ends, respectively. The dashed line indicates the interface of the N- and C-lobes. (B) Primary sequence alignment of TSWV N and BUNV N. Residues in white with red highlighting are identical residues, and residues in red with blue frames are conserved residues. The secondary structures of TSWV N are shown. The residue numbers correspond to TSWV N.
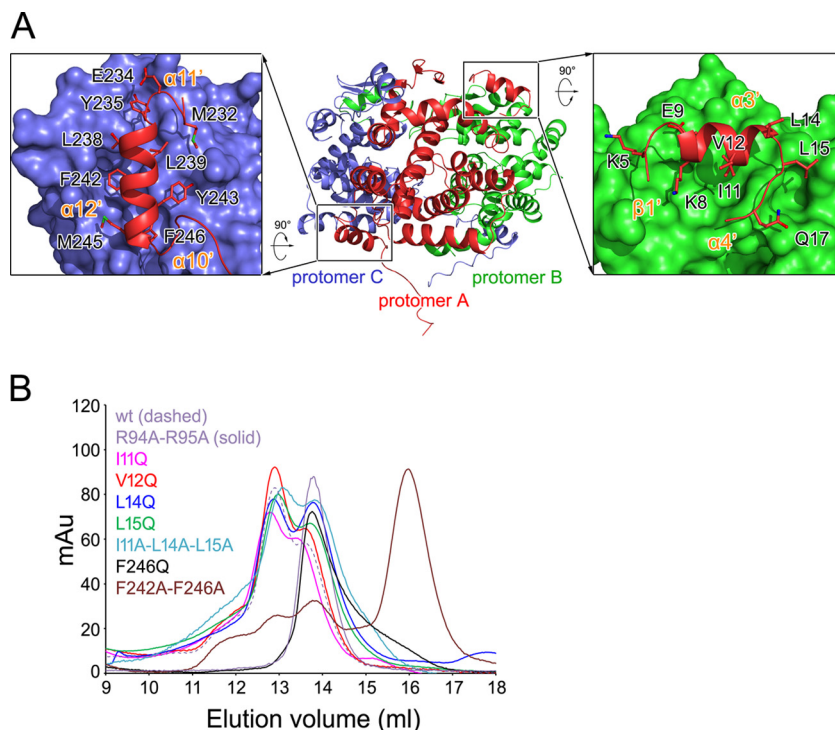
FIG 4 Interprotomer interactions. (A) Three adjacent TSWV N protomers are shown as cartoons in red, green, and blue. The contact of the N-terminal arm of protomer A with the N-lobe of protomer B and the contact of α13 in the C-terminal arm of protomer A with the C-lobe of protomer C are framed and detailed in enlarged insets. (B) Key residues on the interprotomer interface were mutated, and the recombinant proteins were analyzed by SEC by using a Superdex-200 10/300 column. The lines indicate absorbance at 280 nm.

To further characterize a function of these residues at the homotypic interface, we replaced the interacting residues and evaluated whether these mutations disrupted the homotypic interaction in gel filtration. We first mutated residues I11 and L14 to Gln or Ala, either alone or in combination (Fig. 4B). Because the interprotomer interaction at the N terminus is constituted by a variety of molecular interactions, mutations on specific single residues may not affect their interaction. We also tried to produce N-terminal truncations and examine the effect on homotypic contact; however, no sufficient amounts of recombinant protein could be expressed. We reasoned that the truncations on the N terminus may affect the correct folding of TSWV N. Previous studies have demonstrated that the N-terminal truncations obviously affect N-N interaction in a yeast two-hybrid system (26), supporting our structural observations. Moreover, an F242A F246A double mutation at the C-terminal arm completely eliminated N oligomers. Interestingly, though the single mutation F246Q did not affect the trimeric N, the higher-order oligomer could not be observed in gel filtration. Collectively, these results support a model with both N- and C-terminal arms contributing to the oligomerization of TSWV N.

Homotypic contact between the TSWV N trimers. An interesting observation in the TSWV N structure was an additional interprotomer interaction between two N trimers from adjacent ASUs (Fig. 5). The interaction is contributed by the C terminus of protomer A in one ASU with the N-lobe of protomer B in another ASU and the C terminus of protomer C in one ASU with the N-lobe of protomer C in the third ASU. Because these two interaction regions are strictly identical, we used one of them to represent both in the following discussion. The interaction area on the surface of the protomer in the adjacent ASU is located at the interface of the N- and C-lobes on the reverse side of the RNA binding groove. The residues Q208, K211, and Y215 in α12, R141 in α8, and V105 in α5 constitute an elaborate hydrogen bond network with the
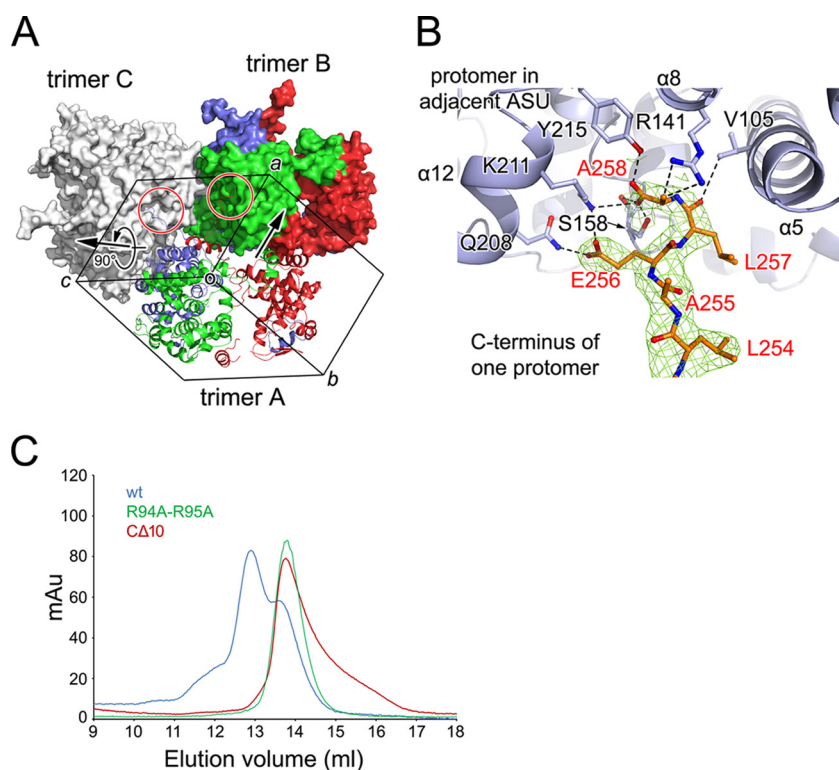
FIG 5 Unique homotypic interaction at the C terminus of the N protomer. (A) The ring-shaped trimers in three adjacent crystallographic ASUs are shown. The protomers in one ASU are displayed as cartoons in red, green, and blue. The protomers in another ASU are displayed as molecular surfaces in colors. The protomers in a third ASU are displayed as white surfaces. The unit cell is within the black lines. Trimer B is a single translation of trimer A along the crystallographic *a* axis, while trimer C is the 90° rotation combined with a translation of trimer along the crystallographic *c* axis. The intertrimer interacting regions are highlighted by red circles. (B) Details of the intertrimer interaction region. The C terminus of one protomer is shown as colored sticks, and the interacting protomer is shown as a blue cartoon. The key residues for intertrimer interaction are shown as colored sticks. An omit 2*Fo-Fc* map around the C terminus of one protomer is displayed at 1.0 σ. Hydrogen bonds are indicated by dashed lines. (C) The last 10 C-terminal residues were truncated, and the recombinant protein was analyzed by SEC using a Superdex-200 10/300 column. The lines indicate absorbance at 280 nm.

C terminus of a protomer in another ASU and thus stabilize it. The hydroxyl atoms of the E256 create a hydrogen bond with the Nε2 atom of Q208′ (a prime indicates the residue in the adjacent protomer) and the Nζ atom of K211′. The carbonyl atom of A258 interacts with the Nζ atom of K211′, the carbonyl atom of S158′, and the hydroxyl atom of S158′. Moreover, the carboxyl oxygen of A258 contacts the hydroxyl group of Y215′, and the C$_\beta$ atom of A258 is further stabilized by an interaction with the side chain of R141′. An additional hydrogen bond between the carbonyl atom of L257 and the Cγ atom of V105′ was also observed. The robust electron density of the C-terminal residues indicates there is a strong interoligomer interaction. A very interesting observation is that the lack of 10 C-terminal residues (CΔ10) does not affect the trimerization of TSWV N but clearly eliminates the higher-order oligomer. This is also consistent with previous studies of a TSWV N homotypic interaction in a yeast two-hybrid system (26). We thus propose that this unique interaction at the C termini may play a unique role in the formation of TSWV RNP in the virus life cycle.

RNA binding groove. The body parts and the RNA-binding grooves in the three TSWV N protomers have extremely high structural conservation, with a 0.6-Å RMSD of Cα atoms of 170 aligned residues (Fig. 3A). The RNA binding groove is clamped by N- and C-lobes (Fig. 6A). α2 and α5 constitute the ceiling, whereas α10 and α11 form the floor of this groove. Additionally, a loop region (residues M145 to L150) connecting α8 and α9 is presented as the inner wall.
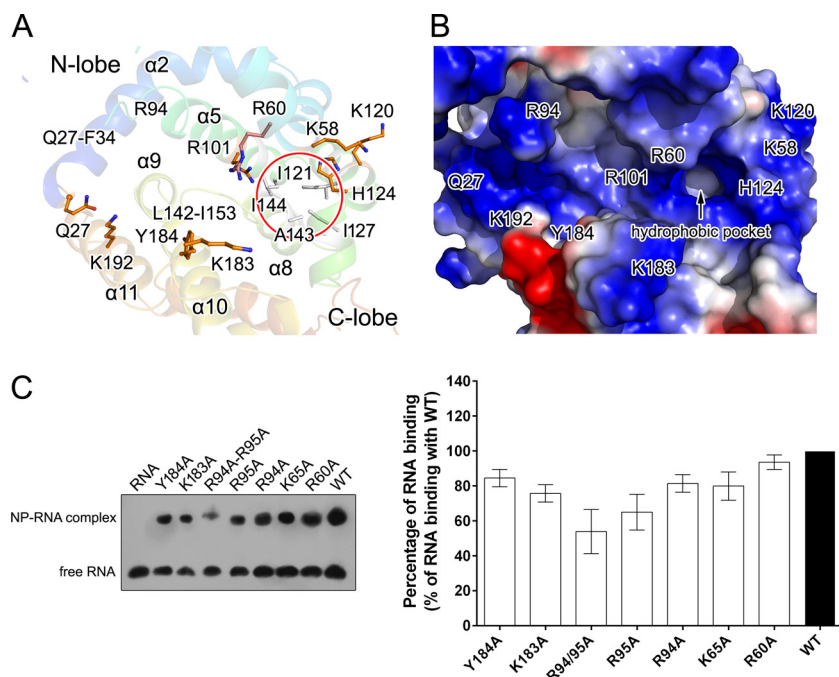
FIG 6 RNA binding groove of TSWV N. (A) The residues forming the RNA-binding groove are displayed as colored sticks. The featured hydrophobic deep groove is highlighted by a red circle. (B) Electrostatic surface potential of the RNA-binding groove. Positive potential is shown in blue ($+5$ kT/e), and negative potential is in red (-5 kT/e). The image was drawn using PyMOL (39). The residues that provide positive charges are labeled. The deep hydrophobic pocket is labeled. (C) Impacts of different mutations on RNA binding. Key residues in the RNA-binding groove were mutated, and their RNA-binding affinities were measured by EMSA. The left panel is one representative original result of three independent experiments. The calculated RNA-binding abilities compared with those of the WT protein are shown in the right panel.

Prior research has shown that the basic residues of the viral N provide positive charges that enable interactions with the phosphate moieties of ligand-bound nucleic acids. The positively charged residues in the RNA-binding groove of TSWV N include K58, R60, R101, K120, H124, K183, and K192 (Fig. 6A). All of these residues are highly conserved throughout all tospoviruses (25), which indicates that there is an identical mechanism of RNA encapsidation. To verify the impacts of these residues on RNA binding, we performed electrophoretic mobility shift assays (EMSAs) by using a 15-nucleotide (nt) ssRNA as a probe (Fig. 6C). Results show that the individual substitutions of alanine residues for K183, Y184, R94, R95, and K65 reduce the RNA-binding ability by 70% to 80% of WT TSWV N, whereas the mutation R60A displays a very slight effect. To be consistent with a previous report (25), the R94A R95A double mutation significantly attenuates RNA binding to 50% of that of the WT protein, supporting their crucial role in RNA binding of TSWV N.

Previous structural studies show that the N proteins encoded by bunyaviruses in the *Orthobunyavirus*, *Phlebovirus*, and *Hantavirus* genera feature a deep hydrophobic pocket inside the RNA-binding groove to sequester several RNA bases, which is distinct from other viral N proteins (3, 6, 15). Similarly, we found a remarkably deep hydrophobic pocket that is constituted by the hydrophobic residues I121, I127, A143, and I144 in the RNA-binding groove (Fig. 6A and B). This pocket is very similar to the hydrophobic pocket in RVFV N (6) and in BUNV N (3, 11). This result may reflect a unique RNA encapsidation mechanism of bunyavirus compared to that of other −ssRNA viruses. However, a hydrophobic pocket could not be observed in nairovirus N (2, 31).

DISCUSSION

In this study and others, the structures of N proteins encoded by the members of the five bunyavirus families have been successfully determined. Except for nairovirus N, all

reported bunyaviral N proteins possess N- and C-lobes that face each other to form a positively charged groove for RNA binding, but they use different mechanisms to employ homotypic interactions for forming high-order RNPs. Among them, the core regions of the orthobunyavirus, phlebovirus, hantavirus, and tospovirus N proteins present bona fide structural homologies, and they all use arms in their N- and/or C termini for oligomer formation and encapsidate RNA in a positively charged groove. In contrast, nairovirus N (2) has no structural similarity with other bunyaviral N proteins but is highly conserved, with N encoded by arenavirus (32). Furthermore, in nairovirus N, the head part of one protomer interacts with the tail part of an adjacent protomer, whereas in orthobunyavirus-, phlebovirus-, hantavirus-, and tospovirus-encoded N proteins, the head domain of one protomer interacts with the head domain of an adjacent protomer and the tail domain of this protomer interacts with the tail domain of other adjacent protomer (33). This structural information suggests that evolutionary relationships exist between orthobunyavirus, phlebovirus, hantavirus, and tospovirus, and it also implies that nairovirus is evolutionarily closer to arenavirus rather than to bunyavirus, as reported by Carter et al. (9).

A set of studies has been conducted in the past decade on TSWV N to determine its biological function and biochemical properties. The first attempt to map the functional domains of TSWV N for multimerization showed that both the N-terminal end (amino acids 1 to 39) and the C-terminal end (amino acids 233 to 248) were important for oligomerization (26), which is clearly consistent with the structural and biochemical results presented here. In the same study, two phenylalanines, F242 and F246, which are highly conserved in the N protein within the *Tospovirus* genus (Fig. 7) were shown to play a crucial role in homotypic interaction (26). In the structure of TSWV N, the hydrophobic side chains of F242 and F246 are buried in the deep pocket in the C-lobe of an adjacent protomer (Fig. 5), which is consistent with their critical role in N homotypic interactions. Meanwhile, another study showed that the TSWV N proteins with truncations spanning residues 1 to 127, residues 128 to 258, and residues 190 to 258 bind with probe RNA, but the TSWV N protein with a truncation covering residues 128 to 190 cannot (27). This result is also consistent with the structure in NN (residues 1 to 127), NC (residues 128 to 258), N4 (residues 190 to 258) that covers the residues to form an RNA-binding groove, but N4 is distant from the groove. In a subsequent investigation, a filter binding assay with digoxigenin (DIG)-labeled RNA as the probe and an RNase resistance assay revealed the impacts of individual residues on RNA encapsidation (25). R60, K65, K68, K81, K192, and T195 of TSWV N had little influence, but R94, R95, K183, and Y184 were important for N binding to RNA. In the structure, the positive side chains of R94 and K183 are in the RNA-binding groove, and Y184 is involved in the formation of the bottom of the RNA-binding groove. However, R95 faces the reverse side of the RNA-binding groove and is completely buried in the N-lobe to interact with α2. We propose that the mutation of R95 to an alanine residue may affect the overall folding of TSWV N and may ultimately impact RNA binding.

Many previous structural studies on viral N proteins suggest that the oligomeric architecture obtained in the crystal reflects the most abundant state of the recombinant protein expressed and purified *in vitro* and that the monomer-sized N-RNA complex is most likely the building block to form the linear RNP that will be further packed with helical symmetry during the process of virus assembly and packaging (reviewed in reference 34). All other reported bunyavirus N proteins interact only with adjacent protomers for the formation of higher-order RNP and do not have cross-ASU homotypic interactions. In the structure of TSWV N, it is interesting to find that the C terminus was extended after α13 of each protomer and formed an additional contact with the interface of the N- and C-lobes of every other protomer while α13 of the same protomer interacted with the C-lobe of an adjacent protomer in the same ASU. This additional contact suggests that there is a distinct mechanism for the formation of TSWV RNP that helps to make RNP more stable during the unique cell-to-cell transport of TSWV as a plant-infecting virus. While this report was in revision, Komoda et al. published and deposited their TSWV N coordinate (35). The body parts, RNA-binding
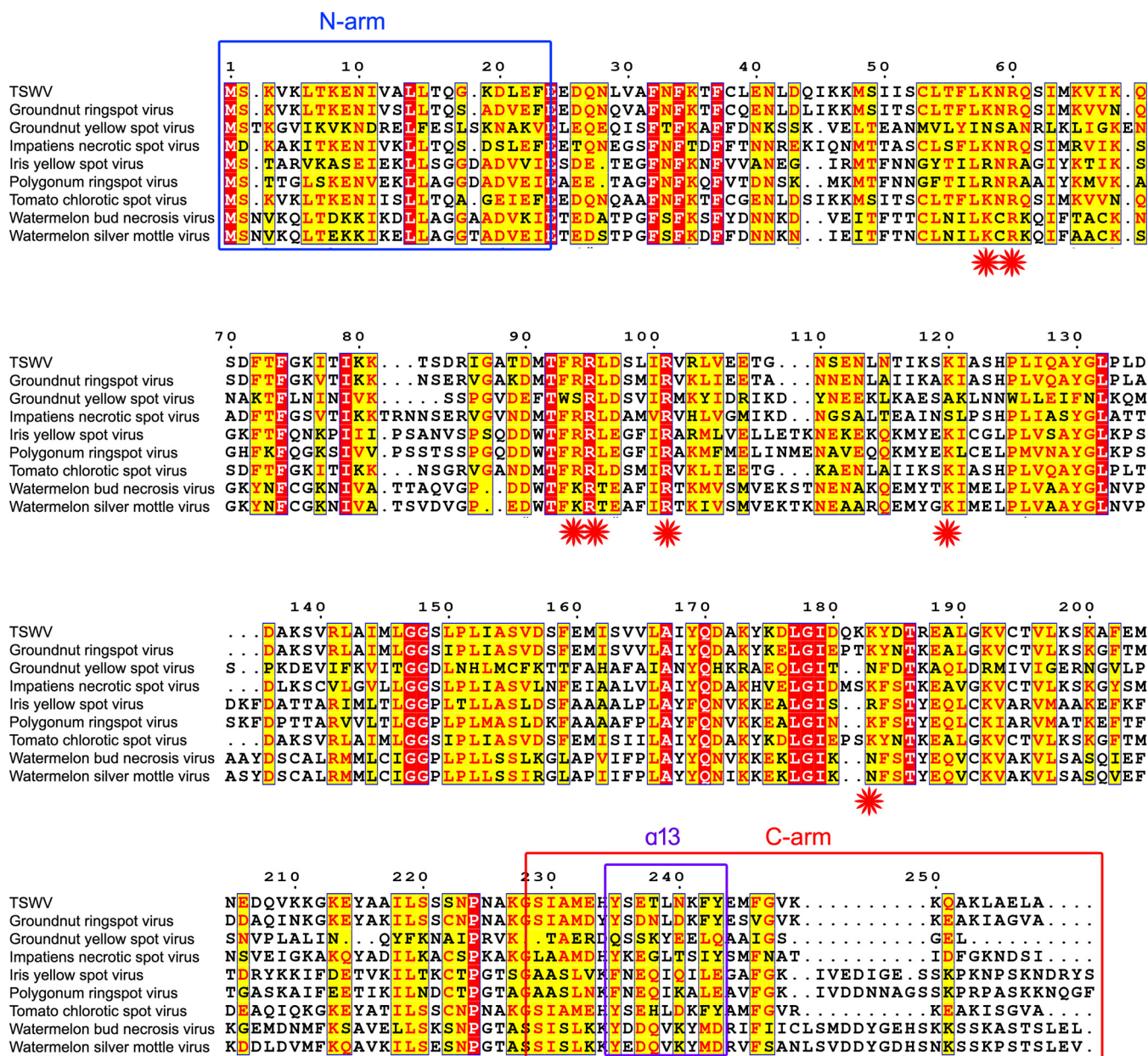
FIG 7 Sequence alignment of tospovirus-encoded N proteins. ClustalW was used for the multiple alignment of tospovirus-encoded N proteins, including those of TSWV, groundnut ringspot orthotospovirus (AAF64317), groundnut yellow spot orthotospovirus (AEK28764), impatiens necrotic spot orthotospovirus (AAA47944), iris yellow spot orthotospovirus (ANS14441), polygonum ringspot orthotospovirus (ABO31117), tomato chlorotic spot orthotospovirus (AJW82846), watermelon bud necrosis orthotospovirus (ACH91860), and watermelon silver mottle orthotospovirus (AIU47371). Residues with a red background are identical, whereas residues with a yellow background are conserved. The residue numbers correspond to those of TSWV N. Positions of key residues for RNA binding on TSWV N are labeled with flower-like red asterisks. N- and C-terminal arms and α13 are framed.

groove, and interprotomer interactions observed in our structure are highly identical to the structure deposited by Komoda et al., providing validation for the results reported here. In contrast, the C-terminal end, which employs an intertrimer homotypic interaction, presents distinct conformations in the structures reported by our group and Komoda et al., although an intertrimer homotypic interaction can be observed in both structures. This is likely to be a result of the different crystallographic packing and indicates the flexibility of this C-terminal end during the formation of virus RNP.

MATERIALS AND METHODS

Protein production. Codon-optimized cDNA for full-length tomato spotted wilt virus nucleoprotein (TSWV N; residues 1 to 258) was synthesized by GENEWIZ. The DNA amplicon was digested with BamHI

TABLE 2 Data collection and refinement statistics

Parameter	Value for:	
	Native	Se-MAD peak
Date collection statistics		
Cell parameters		
a (Å)	55.4	55.8
b (Å)	76.5	76.3
c (Å)	98.4	96.5
α, β, γ (°)	90.0, 93.6, 90.0	89.9, 89.9, 90.0
Space group	$P2_1$	$P1$
Wavelength used (Å)	0.9798	0.9798
Resolution (Å)	50.0–2.8 (2.85–2.80)[c]	50.0–3.9 (3.97–3.90)[c]
No. of all reflections	134,384 (6,045)	49,305 (2,488)
No. of unique reflections	20,050 (973)	14,260 (754)
Completeness (%)	99.9 (99.8)	100.0 (100.0)
Average $I/\sigma(I)$	21.1 (4.6)	21.2 (1.6)
$R_{merge}{}^a$ (%)	7.2 (47.1)	6.1 (28.6)
$R_{pim}{}^a$ (%)	3.0 (19.4)	2.2 (15.3)
CC1/2^a (%)	99.8 (92.1)	99.9 (95.4)
Refinement statistics		
No. of reflections used [$\sigma(F) > 0$]	19,805	
$R_{work}{}^b$ (%)	23.0	
$R_{free}{}^b$ (%)	26.9	
RMSD bond distance (Å)	0.009	
RMSD bond angle (°)	1.412	
Average B value (Å²)	42.2	
No. of protein atoms	5,731	
No. of solvent atoms	24	
Ramachandran plot		
Res. in favored and allowed regions (%)	99.4	
Res. in outlier regions (%)	0.6	
MolProbity score	86th percentile (N = 138, 2.811 Å $\pm$ 0.25 Å)	

$^a R_{merge} = \Sigma_h \Sigma_l \mid I_{ih} - <I_h> \mid / \Sigma_h \Sigma_l <I_h>$, where $<I_h>$ is the mean of the observations I_{ih} of reflection hours. CC1/2 $= \Sigma(a_i - \overline{a})(b_i - \overline{b})/[\Sigma(a_i - \overline{a})^2 \Sigma(b_i - \overline{b})^2]^{1/2}$; $R_{pim} = \sum_h [1/(n_h - 1)] \sum_l \mid I_{hl} - \langle I_h \rangle \mid / \sum_h \sum_l \langle I_h \rangle$.

$^b R_{work} = \Sigma(\mid\mid F(obs)\mid - \mid F(calc)\mid\mid)/\Sigma\mid F(obs)\mid$; R_{free} is an R factor for a preselected subset (5%) of reflections that was not included in refinement.

^{c}Numbers in parentheses are the corresponding values for the highest-resolution shell.

and XhoI restriction enzymes and cloned into the pGEX-6P-1 expression vector upstream of the glutathione *S*-transferase (GST) tag. The sequences of the primers are as follows: forward, 5'-CGGGATC CATGAGCAAGGTTAAGCTGAC-3'; reverse, 5'-CCCTCGAGTTAGGCCAGCTCGGCCAGT-3'. All mutants, including TSWV N (R94A R95A), were constructed with a site-directed gene mutagenesis kit (TransGen Biotech, China). The validity of these constructs was confirmed by sequencing.

Recombinant wild-type and mutant forms of TSWV N were expressed and purified with a general protocol. Briefly, recombinant plasmids were transformed into *E. coli* strain BL21(DE3) and overexpressed with a GST tag fused at the N terminus. The cells were cultured at 37°C in 800 ml LB medium containing 100 μg/ml ampicillin. Once the OD$_{600}$ reached 0.5 to 0.6, the culture was transferred to 16°C, and protein was induced by incubating cells with 0.25 mM isopropyl-β-D-1-thiogalactopyranoside (IPTG) for an additional 16 h. Harvested cells were resuspended in ice-cold lysis buffer (20 mM HEPES, 500 mM NaCl, pH 7.0) and homogenized with a low-temperature ultra-high-pressure cell disrupter (JNBIO, China). The lysate was centrifuged at 25,000 $\times$ *g* for 30 min at 4°C to remove cell debris. The supernatant was then loaded twice onto a GST column preequilibrated with lysis buffer. The resin was washed four times with 80 ml of lysis buffer, and the GST tag was removed by digestion with PreScission protease (GE Healthcare) at 4°C. The recombinant R94A R95A protein for crystallization was captured on a 1-ml HiTrap heparin column (GE Healthcare) and eluted with a concentration gradient of NaCl. The fraction that peaked at the 330 mM NaCl gradient was pooled and concentrated to 0.5 mg/ml in a buffer containing 20 mM HEPES, 200 mM NaCl, and 5 mM dithiothreitol (DTT), pH 7.0, and was subsequently loaded onto a Superdex-200 10/300 column for further purification. The major peaks spanning the elution volume ranging from 13 to 14.5 ml were collected, concentrated, and again loaded onto a Superdex-200 10/300 column for a second purification. The sample in the single peak was concentrated to 40 mg/ml for crystallization. The protein appeared to be greater than 95% pure according to SDS-PAGE analysis and had an A_{260}/A_{280} ratio of 0.55. The purified protein was flash-frozen in liquid nitrogen and stored at 193 K. The selenomethionine (SeMet) derivate of TSWV N was produced using the same construct and the *E. coli* strain grown in M9 medium containing 50 mg/liter selenomethionine. SeMet-substituted TSWV N was purified under the same conditions used for the wild-type protein.

Crystallization. Initial crystallization trials were performed in a 96-well format using a 1:1 ratio of well solution to protein at 28 mg/ml by screening commercial crystal screening kits at 16°C, including the Index, Crystal Screen, Crystal Screen 2, PEG/Ion, PEG/Ion 2, SaltRX, and Natrix from Hampton Research. Small crystals of TSWV N (R94A R95A) first appeared after 1 day in 0.05 M ammonium sulfate, 0.05 M Bis-Tris (pH 6.5), and 30% (vol/vol) pentaerythritol ethoxylate (15/4 EO/OH). Further optimization with glycerol, $(NH_4)_2SO_4$, and temperature adjustment was performed, and the final optimized crystal conditions were as follows: 0.05 M Bis-Tris (pH 7.0), 22% (vol/vol) pentaerythritol ethoxylate (15/4 EO/OH), 20% (vol/vol) glycerol, with 40 mg/ml recombinant protein at 4°C. The crystals were harvested in a dry nitrogen stream at 100 K for X-ray data collection. SeMet TSWV N (R94A R95A) crystals were grown under the same conditions.

X-ray data collection, processing, and structure determination. Data were collected under cryogenic conditions at 100 K. The selenomethionine SAD data set of TSWV N (R94A R95A) was collected at 3.9 Å using a wavelength corresponding to the Se peak at the SSRF (Shanghai, China) beamline BL19U, and another native data set was collected at 2.8 Å. All data sets were indexed, integrated, and scaled by using the HKL2000 package (36). All crystals belonged to the space group $P2_1$ with the cell parameters $a = 55.4$ Å, $b = 76.5$ Å, $c = 98.4$ Å, and $\beta = 93.6°$. The SAD data phases were calculated and substantially improved by solvent flattening using the PHENIX program (19). A model was manually built into the modified experimental electron density using COOT (37) and further refined in PHENIX. Model geometry was verified using the program MolProbity (38). The final refinement statistics are summarized in Table 2. All structure figures were drawn with PyMOL (39).

AUC analysis. Analytical ultracentrifugation (AUC) was performed at 4°C and 42,000 rpm using an XL-I analytical ultracentrifuge (Beckman Coulter, USA). Four hundred microliters of purified TSWV N protein at a concentration of 3 mg/ml in the buffer containing 20 mM HEPES, 200 mM NaCl, and 5 mM DTT, pH 7.0, was loaded on an analytical ultracentrifuge for the assay. The migration of TSWV N protein was monitored at a wavelength of 280 nm. The sedimentation velocity data were analyzed and calculated using SEDFIT software (40).

EMSA. An electrophoretic mobility shift assay (EMSA) was performed to clarify the RNA binding feature of TSWV N, by using a general protocol and a commercial EMSA kit (Beyotime, Haimen Institute of Biotechnology, China). A biotin-labeled ssRNA probe derived from the 5' UTR of the TSWV S segment, 15 nt in length, was synthesized by TaKaRa Biotechnology (Dalian, China). Four micromolar WT N or the mutated proteins were incubated with 2 μM ssRNA probe in a 10-μl reaction mixture. After a 30-min incubation on ice, the reaction mixture was separated in a 10% native polyacrylamide gel with 0.5× TBE (Tris-Borate-EDTA), and then the gel was transferred and UV-cross-linked for 20 min onto a nylon membrane (Beyotime, Haimen Institute of Biotechnology, China). Bands were detected by a probe biotin-labeling kit (Beyotime, Haimen Institute of Biotechnology, China).

Accession number(s). The coordinates and structure factors for TSWV N have been deposited at the RCSB under accession code 5Y6J.

REFERENCES

1. Plyusnin A, Beaty BJ, Elliott RM, Goldbach R, Kormelink R, Lundkvist Å, Schmaljohn CS, Tesh RB. 2010. Bunyaviridae, p 693–709. In King AMQ, Lefkowitz EJ, Adams MJ, Carstens EB (ed), Virus taxonomy: classification and nomenclature of viruses. Ninth report of the International Committee on Taxonomy of Viruses. Elsevier, San Diego, CA.

2. Guo Y, Wang W, Ji W, Deng M, Sun Y, Zhou H, Yang C, Deng F, Wang H, Hu Z, Lou Z, Rao Z. 2012. Crimean-Congo hemorrhagic fever virus nucleoprotein reveals endonuclease activity in bunyaviruses. Proc Natl Acad Sci U S A 109:5046–5051. https://doi.org/10.1073/pnas.1200808109.

3. Li B, Wang Q, Pan X, Fernandez de Castro I, Sun Y, Guo Y, Tao X, Risco C, Sui SF, Lou Z. 2013. Bunyamwera virus possesses a distinct nucleocapsid protein to facilitate genome encapsidation. Proc Natl Acad Sci U S A 110:9048–9053. https://doi.org/10.1073/pnas.1222552110.

4. Moncke-Buchner E, Szczepek M, Bokelmann M, Heinemann P, Raftery MJ, Kruger DH, Reuter M. 2016. Sin Nombre hantavirus nucleocapsid protein exhibits a metal-dependent DNA-specific endonucleolytic activity. Virology 496:67–76. https://doi.org/10.1016/j.virol.2016.05.009.

5. Ferron F, Li Z, Danek EI, Luo D, Wong Y, Coutard B, Lantez V, Charrel R, Canard B, Walz T, Lescar J. 2011. The hexamer structure of Rift Valley fever virus nucleoprotein suggests a mechanism for its assembly into ribonucleoprotein complexes. PLoS Pathog 7:e1002030. https://doi.org/10.1371/journal.ppat.1002030.

6. Raymond DD, Piper ME, Gerrard SR, Skiniotis G, Smith JL. 2012. Phleboviruses encapsidate their genomes by sequestering RNA bases. Proc Natl Acad Sci U S A 109:19208–19213. https://doi.org/10.1073/pnas.1213553109.

7. Raymond DD, Piper ME, Gerrard SR, Smith JL. 2010. Structure of the Rift Valley fever virus nucleocapsid protein reveals another architecture for RNA encapsidation. Proc Natl Acad Sci U S A 107:11769–11774. https://doi.org/10.1073/pnas.1001760107.

8. Zhou H, Sun Y, Liu M, Wang Y, Liu C, Wang W, Liu X, Li L, Deng F, Guo Y, Lou Z. 2013. The nucleoprotein of severe fever with thrombocytopenia syndrome virus processes an oligomeric ring to facilitate RNA encapsidation. Protein Cell 4:445–455. https://doi.org/10.1007/s13238-013-3901-4.

9. Carter SD, Surtees R, Walter CT, Ariza A, Bergeron E, Nichol ST, Hiscox JA, Edwards TA, Barr JN. 2012. Structure, function, and evolution of the Crimean-Congo hemorrhagic fever virus nucleocapsid protein. J Virol 86:10914–10923. https://doi.org/10.1128/JVI.01555-12.

10. Wang Y, Dutta S, Karlberg H, Devignot S, Weber F, Hao Q, Tan YJ, Mirazimi A, Kotaka M. 2012. Structure of Crimean-Congo hemorrhagic fever virus nucleoprotein: superhelical homo-oligomers and the role of caspase-3 cleavage. J Virol 86:12294–12303. https://doi.org/10.1128/JVI.01627-12.

11. Ariza A, Tanner SJ, Walter CT, Dent KC, Shepherd DA, Wu W, Matthews SV, Hiscox JA, Green TJ, Luo M, Elliott RM, Fooks AR, Ashcroft AE, Stonehouse NJ, Ranson NA, Barr JN, Edwards TA. 2013. Nucleocapsid protein structures from orthobunyaviruses reveal insight into ribonucleoprotein architecture and RNA polymerization. Nucleic Acids Res 41:5912–5926. https://doi.org/10.1093/nar/gkt268.

12. Reference deleted.

13. Reguera J, Malet H, Weber F, Cusack S. 2013. Structural basis for encapsidation of genomic RNA by La Crosse orthobunyavirus nucleoprotein. Proc Natl Acad Sci U S A 110:7246–7251. https://doi.org/10.1073/pnas.1302298110.

14. Dong H, Li P, Elliott RM, Dong C. 2013. Structure of Schmallenberg orthobunyavirus nucleoprotein suggests a novel mechanism of genome encapsidation. J Virol 87:5593–5601. https://doi.org/10.1128/JVI.00223-13.

15. Guo Y, Wang W, Sun Y, Ma C, Wang X, Wang X, Liu P, Shen S, Li B, Lin J, Deng F, Wang H, Lou Z. 2015. Crystal structure of the core region of hantavirus nucleocapsid protein reveals the mechanism for ribonucleoprotein complex formation. J Virol 90:1048–1061. https://doi.org/10.1128/JVI.02523-15.

16. Olal D, Daumke O. 2016. Structure of the hantavirus nucleoprotein provides insights into the mechanism of RNA encapsidation. Cell Rep 14:2092–2099. https://doi.org/10.1016/j.celrep.2016.02.005.

17. Kormelink R, Garcia ML, Goodin M, Sasaya T, Haenni AL. 2011. Negative-strand RNA viruses: the plant-infecting counterparts. Virus Res 162:184–202. https://doi.org/10.1016/j.virusres.2011.09.028.

18. Rotenberg D, Jacobson AL, Schneweis DJ, Whitfield AE. 2015. Thrips transmission of tospoviruses. Curr Opin Virol 15:80–89. https://doi.org/10.1016/j.coviro.2015.08.003.

19. Adams MJ, Lefkowitz EJ, King AMQ, Harrach B, Harrison RL, Knowles NJ, Kropinski AM, Krupovic M, Kuhn JH, Mushegian AR, Nibert M, Sabanadzovic S, Sanfacon H, Siddell SG, Simmonds P, Varsani A, Zerbini FM, Gorbalenya AE, Davison AJ. 2017. Changes to taxonomy and the International Code of Virus Classification and Nomenclature ratified by the International Committee on Taxonomy of Viruses (2017). Arch Virol https://doi.org/10.1007/s00705-017-3358-5.

20. Carrington JC, Kasschau KD, Mahajan SK, Schaad MC. 1996. Cell-to-cell and long-distance transport of viruses in plants. Plant Cell 8:1669–1681. https://doi.org/10.1105/tpc.8.10.1669.

21. Lucas WJ. 2006. Plant viral movement proteins: agents for cell-to-cell trafficking of viral genomes. Virology 344:169–184. https://doi.org/10.1016/j.virol.2005.09.026.

22. Pappu HR, Jones RA, Jain RK. 2009. Global status of tospovirus epidemics in diverse cropping systems: successes achieved and challenges ahead. Virus Res 141:219–236. https://doi.org/10.1016/j.virusres.2009.01.009.

23. Kormelink R, Storms M, Van Lent J, Peters D, Goldbach R. 1994. Expression and subcellular location of the NSM protein of tomato spotted wilt virus (TSWV), a putative viral movement protein. Virology 200:56–65. https://doi.org/10.1006/viro.1994.1162.

24. Storms MM, Kormelink R, Peters D, Van Lent JW, Goldbach RW. 1995. The nonstructural NSm protein of tomato spotted wilt virus induces tubular structures in plant and insect cells. Virology 214:485–493. https://doi.org/10.1006/viro.1995.0059.

25. Li J, Feng Z, Wu J, Huang Y, Lu G, Zhu M, Wang B, Mao X, Tao X. 2015. Structure and function analysis of nucleocapsid protein of tomato spotted wilt virus interacting with RNA using homology modeling. J Biol Chem 290:3950–3961. https://doi.org/10.1074/jbc.M114.604678.

26. Uhrig JF, Soellick TR, Minke CJ, Philipp C, Kellmann JW, Schreier PH. 1999. Homotypic interaction and multimerization of nucleocapsid protein of tomato spotted wilt tospovirus: identification and characterization of two interacting domains. Proc Natl Acad Sci U S A 96:55–60. https://doi.org/10.1073/pnas.96.1.55.

27. Richmond KE, Chenault K, Sherwood JL, German TL. 1998. Characterization of the nucleic acid binding properties of tomato spotted wilt virus nucleocapsid protein. Virology 248:6–11. https://doi.org/10.1006/viro.1998.9223.

28. Holm L, Rosenstrom P. 2010. Dali server: conservation mapping in 3D. Nucleic Acids Res 38:W545–549. https://doi.org/10.1093/nar/gkq366.

29. Niu F, Shaw N, Wang YE, Jiao L, Ding W, Li X, Zhu P, Upur H, Ouyang S, Cheng G, Liu ZJ. 2013. Structure of the Leanyer orthobunyavirus nucleoprotein-RNA complex reveals unique architecture for RNA encapsidation. Proc Natl Acad Sci U S A 110:9054–9059. https://doi.org/10.1073/pnas.1300035110.

30. Olal D, Dick A, Woods VL, Jr, Liu T, Li S, Devignot S, Weber F, Saphire EO, Daumke O. 2014. Structural insights into RNA encapsidation and helical assembly of the Toscana virus nucleoprotein. Nucleic Acids Res 42:6025–6037. https://doi.org/10.1093/nar/gku229.

31. Surtees R, Ariza A, Punch EK, Trinh CH, Dowall SD, Hewson R, Hiscox JA, Barr JN, Edwards TA. 2015. The crystal structure of the Hazara virus nucleocapsid protein. BMC Struct Biol 15:24. https://doi.org/10.1186/s12900-015-0051-3.

32. Hastie KM, Liu T, Li S, King LB, Ngo N, Zandonatti MA, Woods VL, Jr, de la Torre JC, Saphire EO. 2011. Crystal structure of the Lassa virus nucleoprotein-RNA complex reveals a gating mechanism for RNA binding. Proc Natl Acad Sci U S A 108:19365–19370. https://doi.org/10.1073/pnas.1108515108.

33. Wang X, Li B, Guo Y, Shen S, Zhao L, Zhang P, Sun Y, Sui SF, Deng F, Lou Z. 2016. Molecular basis for the formation of ribonucleoprotein complex of Crimean-Congo hemorrhagic fever virus. J Struct Biol 196:455–465. https://doi.org/10.1016/j.jsb.2016.09.013.

34. Zhou H, Sun Y, Guo Y, Lou Z. 2013. Structural perspective on the formation of ribonucleoprotein complex in negative-sense single-stranded RNA viruses. Trends Microbiol 21:475–484. https://doi.org/10.1016/j.tim.2013.07.006.

35. Komoda K, Narita M, Yamashita K, Tanaka I, Yao M. 2 August 2017. The asymmetric trimeric ring structure of the nucleocapsid protein of Tospovirus. J Virol https://doi.org/10.1128/jvi.01002-17.

36. Otwinowski Z, Minor W. 1997. Processing of X-ray diffraction data collected in oscillation mode, p 307–326. In Carter CW, Jr, Sweet RM (ed), Macromolecular crystallography, part A, vol 276. Academic Press, New York, NY.

37. Emsley P, Cowtan K. 2004. Coot: model-building tools for molecular graphics. Acta Crystallogr D Biol Crystallogr 60:2126–2132. https://doi.org/10.1107/S0907444904019158.

38. Chen VB, Arendall WB, III, Headd JJ, Keedy DA, Immormino RM, Kapral GJ, Murray LW, Richardson JS, Richardson DC. 2010. MolProbity: all-atom structure validation for macromolecular crystallography. Acta Crystallogr D Biol Crystallogr 66:12–21. https://doi.org/10.1107/S0907444909042073.

39. DeLano W. 2002. The PyMOL molecular graphics system. DeLano Scientific, Palo Alto, CA.

40. Schuck P, Rossmanith P. 2000. Determination of the sedimentation coefficient distribution by least-squares boundary modeling. Biopolymers 54:328–341. https://doi.org/10.1002/1097-0282(20001015)54:5<328::AID-BIP40>3.0.CO;2-P.